ARTICLE IN PRESS

Ceramics International xxx (xxxx) xxx

Contents lists available at ScienceDirect

Ceramics International

journal homepage: www.elsevier.com/locate/ceramint

Synergistic enhancement of microwave absorption in CNT-NZF-CI/epoxy and carbon black/epoxy nanocomposites through dual-phase structuring

Idza Riati Ibrahim [a,*], Rodziah Nazlan [b], Siti Nor Ain Rusly [c], Fadzidah Mohd Idris [d], Khamirul Amin Matori [e,f], Ismayadi Ismail [f], Ghazaleh Bahmanrokh [g], Muhammad Misbah Muhamad Zulkimi [f], Nor Hapishah Abdullah [h], Muhammad Syazwan Mustaffa [h], Arlina Ali [c]

[a] Centre for Pre-University Studies, Universiti Malaysia Sarawak, 94300, Kota Samarahan, Sarawak, Malaysia
[b] Faculty of Industrial Sciences and Technology, Universiti Malaysia Pahang Al-Sultan Abdullah, Lebuh Persiaran Tun Khalil Yaakob, 26300, Kuantan, Pahang, Malaysia
[c] Faculty of Bioengineering and Technology, Universiti Malaysia Kelantan, Jeli Campus, Jeli, Kelantan, 17600, Malaysia
[d] Advanced Technology and Sustainability Unit, Kolej PERMATA Insan, Universiti Sains Islam Malaysia, Bandar Baru Nilai, 71800, Nilai, Malaysia
[e] Department of Physics, Faculty of Science, Universiti Putra Malaysia, UPM, 43400, Serdang, Selangor, Malaysia
[f] Institute of Nanoscience and Nanotechnology, Universiti Putra Malaysia, UPM, 43400, Serdang, Selangor, Malaysia
[g] School of Materials Science and Engineering, UNSW Sydney, NSW, 2052, Australia
[h] Low Dimensional Materials Research Centre (LDMRC), Dept of Physics, Faculty of Science, University Malaya, 50603, Kuala Lumpur, Malaysia

ARTICLE INFO

Handling Editor: Dr P. Vincenzini

Keywords:
Radar absorbing materials
Carbon nanotubes
Ferrite
Microwave absorption

ABSTRACT

An efficient microwave absorber is essential for reducing electromagnetic interference in modern technologies. Here we highlight a magnetic-catalyst-assisted route to carbon nanotubes (CNTs): CNTs were grown by CVD using Ni–Zn ferrite/carbonyl iron (NZF/CI) as magnetic catalysts, embedding magnetic nanophases within the CNT network. This magnetic–dielectric coupling increases magnetic loss (μ'') through natural-resonance and eddy-current pathways. When combined with a graded double-layer structure which CNT/epoxy (matching/front) and carbon black (CB)/epoxy (absorbing/back), synergistically optimizing impedance matching and in-layer attenuation across the X- and Ku-bands. Single-layer CNT/epoxy and double-layer CNT/epoxy–CB/epoxy nanocomposites were fabricated and characterized by Raman spectroscopy, field emission scanning electron microscopy (FESEM), and a PNA network analyzer over the X- and Ku-band frequency ranges. Results revealed that the optimized double-layer structure, comprising a 1 mm CNT as a matching layer and a 1 mm carbon black as an absorbing layer, achieved a −10 dB absorption bandwidth of 2.58 GHz and over 99.99 % absorption at 11.14 GHz. Microstructural analysis shows nanosized CB (∼41 nm) uniformly distributed, providing abundant interfacial sites and micro-capacitive contacts that elevate ε'', while entangled CNTs (outer diameter ∼61 nm; spiral/twisted/net-like) promote multiple internal reflections and efficient dissipation. The close contact between CNTs and NZF/CI further strengthens magnetic loss and stabilizes impedance matching. These results demonstrate a cost-effective, magnetic–dielectric double-layer strategy for high-performance and thin microwave absorbers.

1. Introduction

Electromagnetic (EM) pollution and interference arising from the rapid proliferation of radars, wireless communication systems, and other electronic devices have become critical global concerns. Prolonged exposure to EM radiation not only threatens human health but also disrupts the performance of sensitive electronic equipment. To mitigate these issues, microwave absorbing materials (MAMs) are widely studied as effective solutions for suppressing unwanted electromagnetic signals. An efficient MAM should exhibit strong absorption, a lightweight structure, thin thickness, and broadband performance, tunable absorption frequencies, ease of processability, and cost-effectiveness [1,2].

---

* Corresponding author.
E-mail address: iiriati@unimas.my (I.R. Ibrahim).

https://doi.org/10.1016/j.ceramint.2025.11.196
Received 29 August 2025; Received in revised form 30 October 2025; Accepted 13 November 2025

Please cite this article as: Idza Riati Ibrahim et al., *Ceramics International,* https://doi.org/10.1016/j.ceramint.2025.11.196

However, simultaneously achieving all these requirements remains a significant challenge and significant research efforts have been dedicated to designing materials that meet these requirements, and various absorbing materials have been developed for effective EM wave absorption [2–5].

The absorption performance of MAMs depends largely on their dielectric and magnetic properties, expressed through the complex permittivity ($\varepsilon^* = \varepsilon' - j\varepsilon''$) and permeability ($\mu^* = \mu' - j\mu''$) [6]. The real components represent energy storage, while the imaginary components correspond to energy dissipation through mechanisms such as conduction and resonance losses. To optimize absorption, materials must exhibit balanced dielectric and magnetic losses for effective impedance matching. Various strategies have been explored to improve microwave absorption efficiency, including the combination of multiple absorbers [7], multi-layered structures [8,9] and chemical modification of absorbents [10]. Despite these advances, designing lightweight absorbers with wideband absorption and high efficiency remains a demanding research focus.

Ferrite-based materials have long been considered promising microwave absorbers due to their high permeability, chemical stability, and magnetic loss characteristics [11–14]. Nevertheless, their high density, brittleness, and limited bandwidth which constrained by the Snoek limit and natural resonance, restrict their practical applications especially at higher frequencies (X- and Ku-bands). Therefore, the application of ferrite-based such as nickel zinc ferrite (NZF) as a microwave absorber is generally limited to lower frequency ranges [15]. In addition, their intrinsic performance remains limited by poor impedance matching and a single magnetic loss mechanism [16,17]. Consequently, the absorption bandwidth of pure ferrite materials tends to be narrow requirement and require thick thickness (6–8 mm) for effective absorption [18]. To address these challenges, extensive research has focused on modifying ferrite-based materials through structural and compositional enhancements. Current research has increasingly focused on hybrid structures that integrate ferrites with lightweight carbon-based materials [19–22].

Among carbon-based materials, carbon nanotubes (CNT) have attracted considerable attention owing to their high aspect ratio, excellent electrical conductivity, and strong dielectric loss capability [23–25]. CNT-based composites can effectively attenuate EM waves at low filler concentrations, making them highly attractive for applications such as stealth coatings and microwave anechoic chambers [26]. In particular, multiwalled carbon nanotubes (MWCNT) are of greatest interest due to their relatively low production cost and superior dispersibility in polymer matrices. Their unique tubular structure and high aspect ratio facilitate efficient EM wave absorption through enhanced dielectric loss, interfacial polarization, and multiple scattering mechanisms [27]. Furthermore, when MWCNT are incorporated into multi-layered structures with ferrite-based materials, these hybrid systems can exploit synergistic dielectric–magnetic interactions, leading to improved impedance matching, stronger attenuation, and broader absorption bandwidths [28–30].

Recent benchmarks clarify how impedance matching and thickness–frequency tuning govern strong absorption across carbon–magnetic and oxide systems. Co-doped Ni–Zn ferrite/graphene nanocomposites exhibit dual deep minima whose peak positions follow the quarter-wavelength relation with thickness, underscoring the role of phase-matching at moderate coatings [31]. Hierarchical NiO architectures achieve very deep reflection loss of −65.1 dB at 13.9 GHz with an ~3 GHz X/Ku window around 7.9 mm, illustrating thickness-controlled impedance matching in magnetic–dielectric oxides [32]. Complementarily, $TiO_2/Ti_3C_2T_x/Fe_3O_4$ composites reach −57.3 dB at 10.1 GHz with 1.9 mm thickness by aligning the optimum where $|Z_{in}/Z_0| \approx 1$, demonstrating an ultrathin route when matching and attenuation are co-optimized [33]. Building on these design rules, the present study employs magnetic-catalyst-assisted CNT growth (NZF/CI) and a graded bilayer (CNT-NZF-CI front, CB back) to decouple entrance matching from interior attenuation at a total thickness of 2 mm.

Here we use Ni–Zn ferrite and carbonyl iron (NZF/CI) as magnetic catalysts for growth of CNTs via chemical vapor deposition (CVD). Unlike post-mixed magnetic fillers, this route anchors soft-magnetic nanophases directly on or within the CNT network, creating intimate magnetic–dielectric interfaces at CNT contact sites. The embedded magnetic centers enhance magnetic loss (μ'') via natural-resonance and eddy-current pathways while simultaneously strengthening interfacial polarization at carbon–magnet boundaries. This magnetic-catalyst-induced CNT architecture is a key novelty that enables stronger, more balanced loss at thin total thickness.

A double-layer absorber behaves as a graded-impedance matching structure: reflection at the air/coating interface is minimized when the impedance transition from air to backing is gradual. Practically, the air-facing matching layer should have moderate ε' and limited loss to keep $|Z_{in}/Z_0| \approx 1$, while the subsequent layer should be lossier (higher ε'') to dissipate the transmitted power (attenuation governed by α). Following this rationale, we assign CNT-NZF-CI/epoxy as the matching (front) layer and carbon black (CB)/epoxy as the absorbing (back) layer. To validate the design principle, we also invert the stacking (i.e., CB front/CNT-NZF-CI back) and compare both sequences under identical total thickness, thereby isolating the roles of entrance matching versus interior attenuation in determining reflection loss. For clarity, layer order is reported from air to metal throughout.

CNTs were synthesized by CVD using magnetic nickel zinc ferrite, $Ni_{0.3}Zn_{0.7}Fe_2O_4$ and carbonyl iron (NZF/CI) as magnetic catalysts, anchoring soft-magnetic nanophases on/within the CNT network and thereby enhancing magnetic loss (μ''). The CNTs were then incorporated into an epoxy resin to form a nanocomposite, and a double-layer structure was created by adding a carbon black/epoxy resin layer atop the CNT/epoxy resin layer. To test the graded-impedance concept, we fabricated and compared both layer orders at equal total thickness (e.g., 2 mm: 1 mm + 1 mm): (i) CNT-NZF-CI/epoxy (front, matching) over CB/epoxy (back, absorbing) and (ii) the inverted stack, CB/epoxy (front)

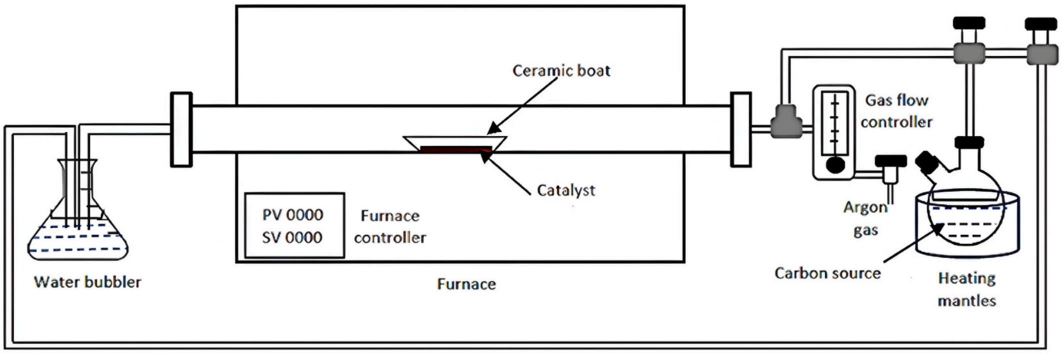

Fig. 1. Diagram of the CVD setup for producing CNTs.

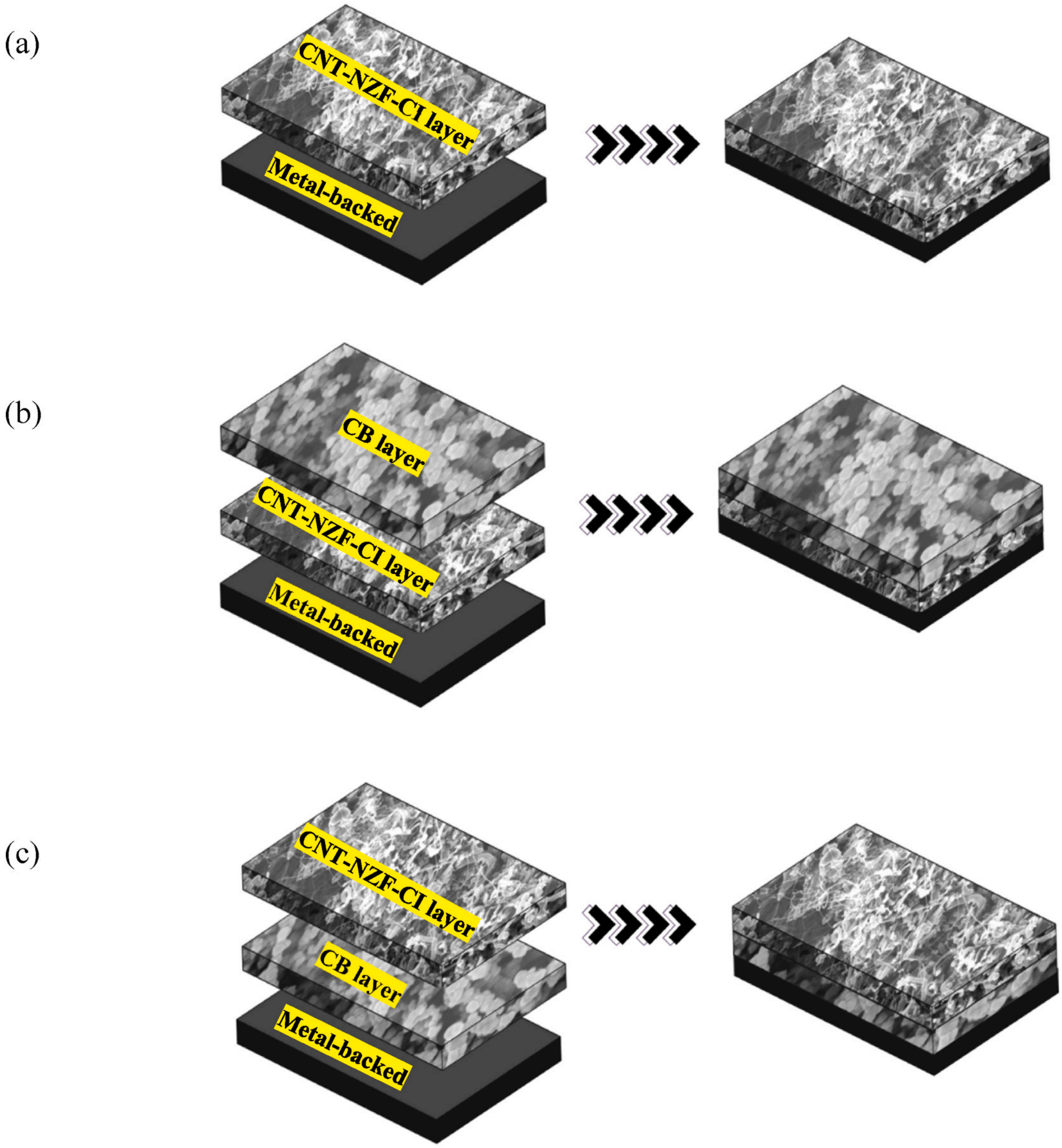

Fig. 2. The layer arrangement for (a) Single-layer composites (CNT-NZF-CI), (b) Multi-layer composites (Carbon Black as matching layer and CNT-NZF-CI as absorbing layer) and (c) Multi-layer composites (CNT-NZF-CI as matching layer and Carbon black as absorbing layer).

over CNT-NZF-CI/epoxy (back). Throughout, layer order is reported from air to metal. This architecture decouples entrance matching from interior attenuation, is benchmarked against a single-layer CNT/epoxy control. This design aims to exploit synergistic dielectric and magnetic losses, reduce material density, and broaden the absorption bandwidth. The dual-phase structuring of CNT/epoxy and carbon black/epoxy nanocomposites offers a cost-effective and high-performance candidate for advanced microwave absorption applications.

Table 1
Description of the layer structure arrangement of the samples.

Samples	Matching layer	Thickness (mm)	Absorbing layer	Thickness (mm)
CNT-NZF-CI 1 mm	–	–	–	1
CB 1 mm/CNT-NZF-CI 1 mm	Carbon black	1	CNT	1
CB 2 mm/CNT-NZF-CI 1 mm	Carbon black	2	CNT	1
CNT-NZF-CI 1 mm/CB 1 mm	CNT	1	Carbon black	1
CNT-NZF-CI 1 mm/CB 2 mm	CNT	1	Carbon black	2

2. Methods

The carbon black used in this study was a commercially available product (TIMCAL C-NERGY™ SUPER C65 Carbon Black). NZF with the composition of $Ni_{0.3}Zn_{0.7}Fe_2O_4$ was synthesized according to the method detailed in our previous work [34]. CNT were synthesized via the chemical vapor deposition (CVD) method, using ethanol as the carbon source. Carbonyl iron (CI) and nickel–zinc ferrite (NZF) were mixed in a 1:1 wt ratio (50 wt% NZF, 50 wt% CI) and used as the catalyst. The mixture was placed in a ceramic boat and positioned at the center of the tube furnace. The furnace tube was purged with argon and the flow was maintained at 100 sccm during heating. The temperature was raised to 700 °C at a rate of 4 $^{\circ}C\ min^{-1}$ and held for 60 min. The ethanol held at 100 °C was vaporized and delivered into the furnace by the argon carrier gas for 30 min. The ethanol decomposed in the hot zone, enabling CNT growth on the catalyst surfaces. After precursor delivery, the furnace was allowed to cool to room temperature before

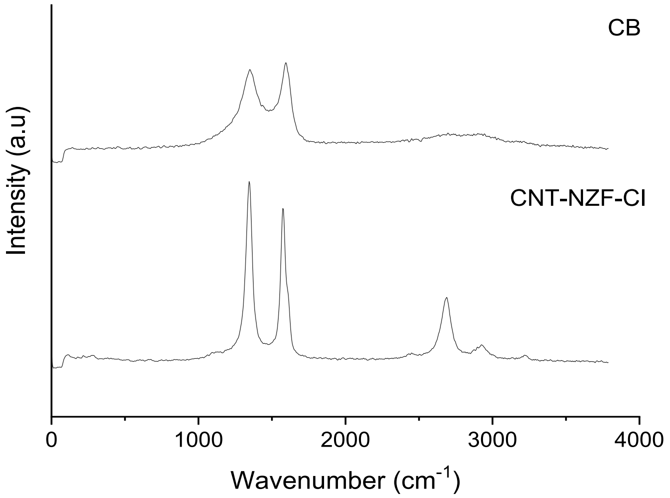

Fig. 3. Raman spectra for carbon black (CB) and CNT grown from $Ni_{0.3}Zn_{0.7}Fe_2O_4$+Carbonyl Iron (CNT-NZF-CI).

the sample was removed for analysis. A schematic of the CVD process is shown in Fig. 1.

CNTs were incorporated into an epoxy matrix at 8 wt% (8 wt% CNT, 92 % epoxy resin). The epoxy resin and hardener were combined at a 10:1 wt ratio, and the CNT/epoxy mixture was vortex-mixed at 3000 rpm for 15–20 min. The resulting mixture was solution-cast into rectangular moulds with target thicknesses of 1, 2, and 3 mm, optimized for X- and Ku-band measurements. All samples were cured at room temperature for 24 h. The layer configurations are illustrated in Fig. 2, while specific thicknesses and layer arrangements are detailed in Table 1.

The structural characterization was conducted using a WITec Alpha 300R Raman Spectrometer, while microstructural features were examined using a NovaNano 230 Field Emission Scanning Electron Microscope (FESEM). Particle size distributions were evaluated using the line intercept method, with more than 200 grains per sample analyzed through Image-J software for statistical accuracy. Electromagnetic properties were measured using an Agilent PNA N5227A Vector Network Analyzer connected to a rectangular waveguide. The transmission line method was employed to evaluate microwave absorption performance within the X- and Ku-band frequency ranges. Complex permittivity and permeability values were derived from the measured scattering parameters using Agilent Technologies 85071E Materials Measurement Software. To assess the influence of layer configuration on microwave absorption behavior, the relative positions of the CNT and carbon black layers were systematically varied. This allowed for a detailed investigation of the effects of matching and absorbing layer placement on overall absorption performance.

3. Results and discussion

The Raman spectra presented in Fig. 3 exhibit two prominent peaks for both carbon black and CNT-NZF-CI samples, located at approximately 1350 cm^{-1} and 1590 cm^{-1}, corresponding to the characteristics D- and G-bands respectively. The D-band near around 1350 cm^{-1} indicative of structural disorder, arising from defects such as vacancies, edge effects, amorphous regions, non-hexagonal ring formations and other imperfections that disrupt the ideal sp^2-hybridized carbon

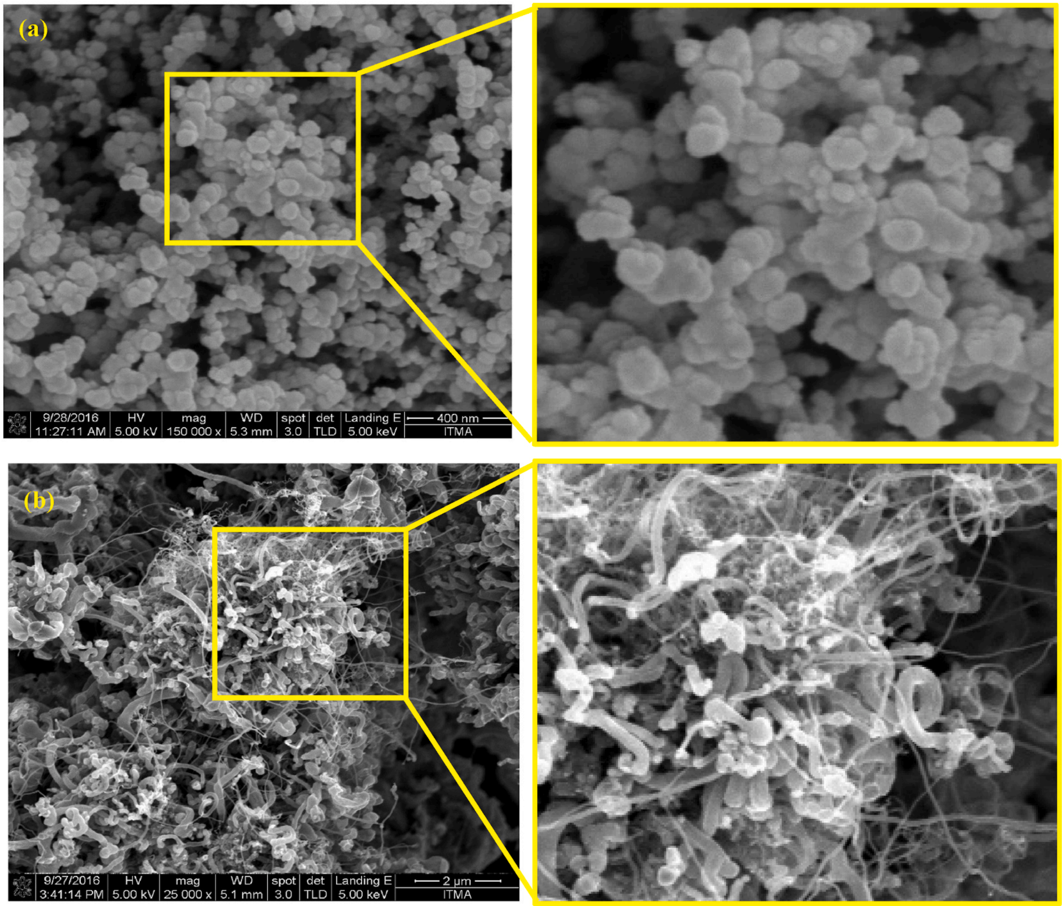

Fig. 4. FESEM images for (a) carbon black (CB) and (b) CNT grown from $Ni_{0.3}Zn_{0.7}Fe_2O_4$+Carbonyl Iron (CNT-NZF-CI).

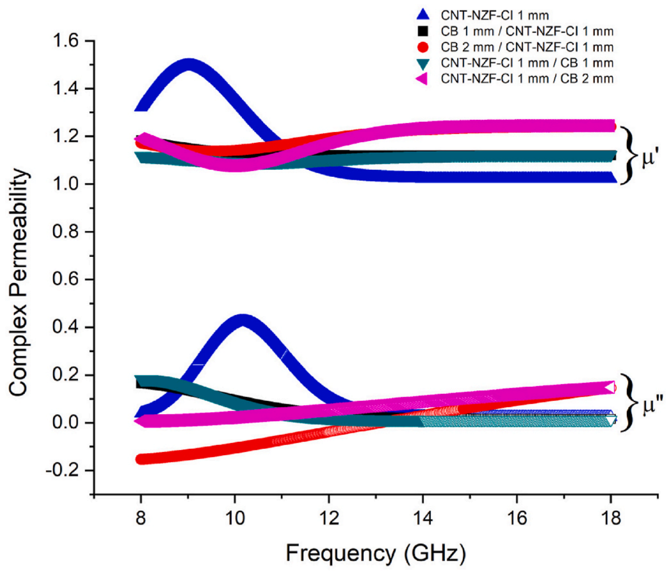

Fig. 5. Complex permeability of single- and double-layer absorbers.

network [35]. In contrast, the G-band observed near 1590 cm^{-1}, originates from the in-plane stretching vibrations of sp2 bonded carbon atoms, and is typically linked to the degree of graphitization ordering in the sample [36]. The Raman D-band (I_D) to G-band (I_G) intensity ratio serves as a common method for gauging the density of structural defects within CNT-NZF-CI, offering a relative indicator of sample structural integrity. This ratio serves as a widely accepted indicator of crystallinity and defect density. Higher I_D/I_G imply greater structural disorder and smaller graphitic domain sizes, while lower I_D/I_G values indicate better graphitic ordering and more crystalline domains. In this study, the I_D/I_G ratio for carbon black is measured at 1.04, indicating a high degree of disorder amorphous carbon material. For the CNT-NZF-CI sample, the ratio is slightly lower at 0.99, reflecting a higher degree of structural order and fewer defects compared to carbon black. This is indicative of the relatively improved graphitic structure in the synthesized CNT-NZF-CI, although some disorder remains due to defects introduced during the CVD synthesis process.

The broadness of both D- and G-bands observed in the spectra further supports the presence of structural disorder, especially in carbon black. These findings align with literature reports, where carbon black typically exhibits broad, overlapping D- and G-bands with I_D/I_G ratios ≥ 1, distinguishing it from more crystalline forms such as graphite [37]. The Raman analysis confirms that both materials exhibit disordered microstructures, with CNT-NZF-CI possessing slightly enhanced structural integrity compared to carbon black. This difference in microstructural quality is expected to influence their respective electromagnetic properties in the final composite system.

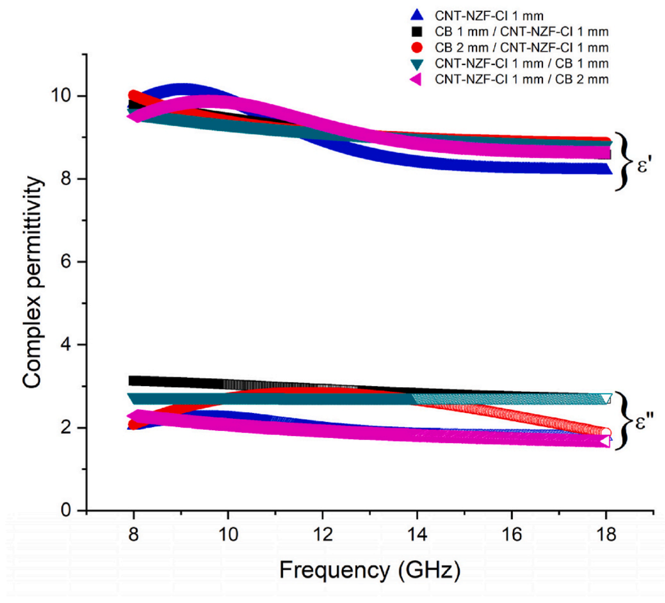

Fig. 6. Complex permittivity of single- and double-layer absorbers.

Fig. 4 shows the microstructure for carbon black and CNT grown from $Ni_{0.3}Zn_{0.7}Fe_2O_4$ and carbonyl iron. The average particle size for carbon black is 41 nm. The microstructure shows uniform shape and distribution of the particles. The nanosized particle offers a high surface-to-volume ratio, significantly enhancing microwave absorption by widening the absorption bandwidth with losses exceeding −10 dB. This enhancement stems from the increased surface area, which facilitated the attenuation of EM waves through improved scattering and reflection. The CNT-NZF-CI sample have an average outer wall diameter of 61 nm, and their microstructure reveals entanglement, with CNT often bundled due to van der Waals forces. The carbon structures exhibit various morphologies, predominantly straight, spiral and twisted, with some net-like fibers formed from the aggregation of fine fibers and particle-like carbon. The presence of hollow, tube-like structures further confirms the tubular nature of the CNT. These unique structures are expected to provide superior EM wave absorption compared to conventional ferrites, primarily due to the multiple internal reflections enabled by the high surface-to-volume ratio [38]. In the composite samples, a closely interconnected network is formed, with short distances between the ends of CNT. Both individual CNT and CNT bundles within the epoxy matrix absorb microwave energy, dissipating radiation through interactions between the internal electrons and external microwave fields.

Several mechanisms were involved when dissipating microwaves as heat inside the material. Microwave absorbers work by enhancing loss mechanisms to absorb electromagnetic wave energy. From Fig. 5, the μ′ of CNT-NZF-CI 1 mm sample ranges from ~1.2 to 1.5 and shows a peak with a maximum value at 9 GHz. While μ″ varies from ~0 to 0.4 and exhibits a peak at 10 GHz. A broad peak from 8 to 12.3 GHZ was observed, somewhat indicating the occurrence of resonance loss, which contributed by $Ni_{0.3}Zn_{0.7}Fe_2O_4$ since CNT were grown from magnetic $Ni_{0.3}Zn_{0.7}Fe_2O_4$ and Carbonyl Iron. When another layer was added to the sample which is 1 mm carbon black, the broad hump disappeared within the range of measured frequency and the μ′ values of CNT-NZF-CI 1 mm/CB 1 mm and CB 1 mm/CNT-NZF-CI 1 mm samples showed almost a constant value of 1.1. However, it is suspected that for the thicker samples, the broad hump due to resonance loss might started to appear earlier below 8 GHz as within the measured frequency, the trend of μ″ decreased with increased frequency up to ~12 GHz, before displaying a constant μ″. The resonant frequency shifts to a lower frequency in relation to the matching layer thickness, t_m as predicted by the following equation:

$$t_m = \frac{nc}{4f_m\sqrt{|\mu_r\varepsilon_r|}}, n = 1, 3, 5\ldots \tag{1}$$

where f_m is the frequency at which the reflection loss is minimum (f_m), μ_r and ε_r are the relative permeability and permittivity.

For the thicker sample with a total thickness of 3 mm, the μ′ values slightly decreased as the frequency increased to 10 GHz, followed by a gradual increase beyond this frequency. The layer arrangement had minimal impact on the overall μ′ trend. The μ'' exhibited negative values up to 13 GHz when carbon black was used as the matching layer, which can be attributed to the system's phase lag between capacitance and inductance, as described by the equivalent circuit model [39]. The magnetic losses, denoted by μ″, are dominant in ferrite which mostly due to spin resonance, with the contribution of eddy currents also being

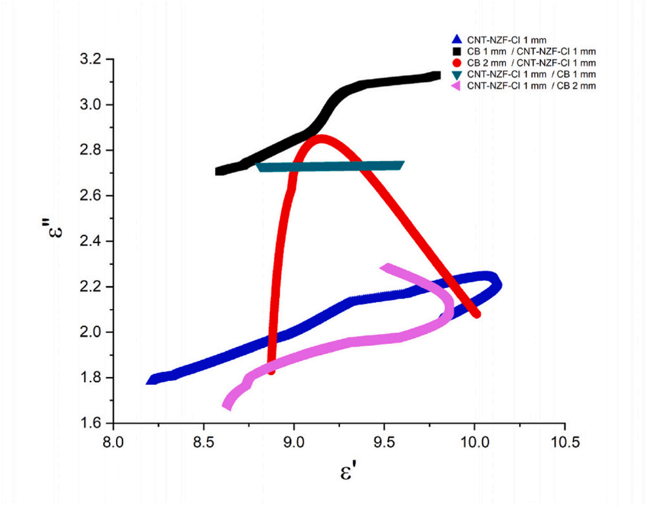

Fig. 7. Dielectric Cole-Cole plot in the frequency range of 8–18 GHz.

frequency-dependent, though not entirely significant [40]. This will be discussed in the next section.

The permittivity in dielectric materials is influenced by four main polarization mechanisms, represented by the equation:

$$P = P_s + P_d + P_a + P_e \tag{2}$$

Where P is the total polarizability, P_s is space charge polarizability, P_d is dipolar polarizability, P_a is atomic polarizability, and P_e is electronic polarizability. The resonant frequencies of electronic and atomic polarizations typically fall within the UV–visible and IR-far IR regions, respectively [40]. Since microwave frequencies are well below these resonant frequencies, the contributions from electronic and atomic polarizations are minimal and relatively frequency-independent. In contrast, space charge and dipolar polarizations play a more significant role at microwave frequencies. In this study, the CNT and carbon black particles were separated by an insulating matrix, introducing heterogeneity into the system. This separation led to the accumulation of space charge at the interfaces, which then caused interfacial polarizations.

Fig. 6 displays the plots of complex permittivity versus frequency measured from our samples, showing peak values of 10.2 for ε' and 3.2 for ε''. The single-layer CNT-NZF-CI 1 mm sample exhibited a broad peak in ε' between 8 and 13 GHz, followed by a nearly constant value beyond 13 GHz. Due to excellent electrical conductivity and high aspect ratio of CNT-NZF-CI, they can readily form conducting networks within the epoxy matrix. These networks interact and effectively attenuate electromagnetic waves. As the frequency increases, the dipoles within the system are unable to realign with the alternating electric field, leading to a reduction in dielectric permittivity, which eventually stabilizes at a constant value. The samples with a total thickness of 2 mm exhibited the highest ε'', indicating the greatest energy loss or dissipation within the system. The ε'' decreased with increased frequency and eventually reached a constant value. There is a slight variation of ε'' when the layers were switched, in which carbon black as the matching layer displayed slightly higher ε''. The dielectric loss showed by ε'' is coherent with the reflection loss as these samples absorbed the maximum electromagnetic wave within the measured frequency.

To clarify which dielectric mechanisms in these carbon-based layered composites, ε'' was analyzed against ε' in Cole–Cole coordinates (Fig. 7), where near-semicircular arcs indicate relaxation processes and depressed or multiple arcs reflect distributed interfacial polarization process, by contrast, distorted, unclosed traces with right-hand oblique tail where ε'' increases sharply at the high-ε' (low-frequency) end, indicating conduction-dominated loss rather than a well-defined relaxation. These features explain the impedance matching

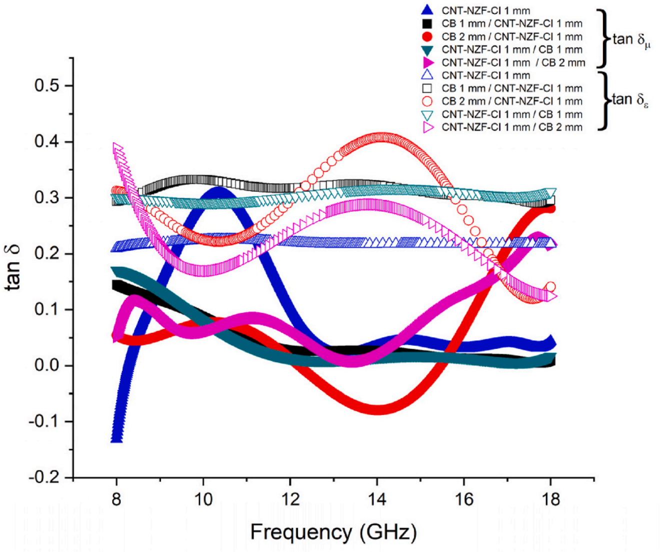

Fig. 8. Magnetic and dielectric loss tangent.

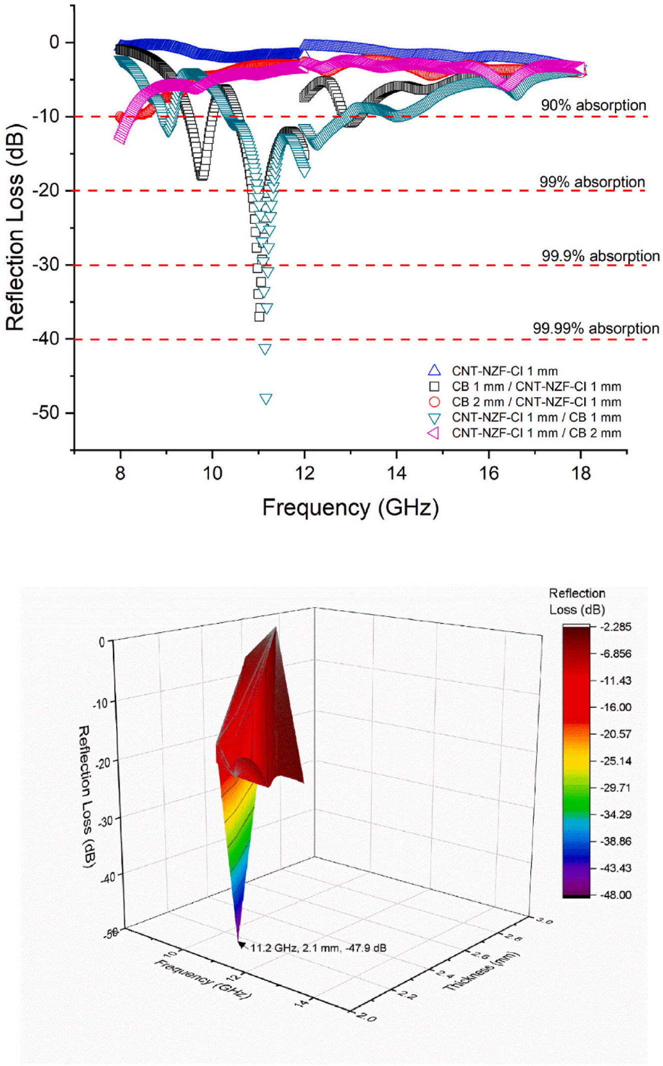

Fig. 9. (a) Reflection Loss for single and double-layer nanocomposites structures **(b)** 3D reflection loss of CNT-NZF-CI 1 mm/CB 1 mm sample.

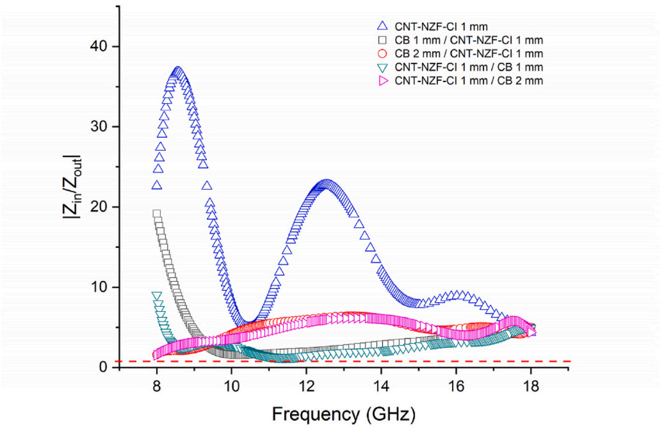

Fig. 10. Normalized input impedance for single and double-layer nanocomposites structures.

and reflection loss observed in Figs. 9 and 10.

Cole–Cole plots (ε'' vs ε') reveal distinct dielectric-relaxation fingerprints across the samples. CB 2 mm/CNT-NZF-CI 1 mm sample exhibits a well-formed single arc ($\varepsilon' \approx 9.2$, $\varepsilon'' \approx 2.85$), indicative of a dominant interfacial relaxation with relatively narrow dispersion, whereas CB 1 mm/CNT-NZF-CI 1 mm sample presents a tail-dominated trace without a closed arc, implying that either (i) a relaxation peak lies outside the measured band, or (ii) a partial conduction network smears the response and prevents arc closure. Both behaviours typical when free-carrier loss starts to compete with polarization loss [41].

CNT-NZF-CI 1 mm/CB 1 mm sample shows minimal in-band dispersion (nearly horizontal strip), consistent with a relaxation positioned beyond 8–18 GHz. In contrast, CNT-NZF-CI 1 mm/CB 2 mm sample features two partially resolved arcs, evidencing overlapping interfacial and dipolar/hopping processes and a broader distribution of relaxation times. The CNT-NZF-CI single layer sample displays a broad arc with a shoulder plus a low-frequency oblique tail, reflecting coexisting interfacial/dipolar polarization with some conduction influence. Collectively, the Cole–Cole plots explain the absorption trends. Samples with a clear single arc (CB 2 mm/CNT-NZF-CI 1 mm) allow predictable tuning of the loss peak. Multi-arcs or depressed traces (CNT-NZF-CI 1 mm/CB 2 mm and single-layer CNT-NZF-CI 1 mm) favour bandwidth broadening provided the air/absorber impedance remains well matched ($|Z_{\text{in}}/Z_0| \approx 1$) [42]. Once the wave enters, energy dissipation is governed by the attenuation constant α. In contrast, tail-dominated cases (CB 1 mm/CNT-NZF-CI 1 mm and CNT-NZF-CI 1 mm/CB 1 mm) offer limited additional loss leverage within the measured band.

To assess the overall contribution of microwave magnetic and dielectric losses in the samples, the magnetic loss tangent, $\tan\delta_\mu$, and dielectric loss tangent, $\tan\delta_\varepsilon$ were plotted in Fig. 8, based on the complex permeability and permittivity data shown in Figs. 5 and 6. The loss tangents were calculated as the ratio of the imaginary component to the real component of permeability and permittivity, respectively, using the following equations:

$$\tan\delta_\mu = \frac{\mu''}{\mu'} \tag{3}$$

$$\tan\delta_\varepsilon = \frac{\varepsilon''}{\varepsilon'} \tag{4}$$

A higher loss tangent value corresponds to greater energy dissipation, indicating a more effective conversion of microwaves into other forms of energy. Therefore, high loss tangent values are desirable for microwave absorbers. On the other hand, low ε' and ε'' values result in poor microwave attenuation, while excessively high values can complicate impedance matching. As shown in Fig. 8, the $\tan\delta_\varepsilon$ values are generally higher than $\tan\delta_\mu$. This significant difference indicates that dielectric loss plays a dominant role in the attenuation of EM energy across the frequency range. Most of the plots indicate an imbalance between $\tan\delta_\varepsilon$ and $\tan\delta_\mu$. However, it can be observed that the value distributions for both CB 1 mm/CNT-NZF-CI 1 mm and CNT-NZF-CI 1 mm/CB 1 mm samples demonstrate effective complementarities between permittivity and permeability. This indicates better electromagnetic matching and thus high microwave absorption performance.

Therefore, based on the above discussion, two dominant loss mechanisms can be deduced.

i. Dielectric. In the ε''–ε' Cole–Cole plot, closed or weakly depressed arcs indicate in-band interfacial and dipolar or hopping relaxations, whereas unclosed right-hand tails indicate conduction influence or a relaxation centred outside the measured band. CB-containing samples show the larger arcs, hence interfacial polarization dominates within 8–18 GHz.
ii. Magnetic. A $\mu''(f)$ shoulder with a concurrent $\mu'(f)$ kink signals natural resonance of soft-magnetic nanophases, and by evaluating eddy-current parameter $C_0 = \mu''/(\mu'^2 f)$, an approximately flat C_0 indicates eddy-current loss contribution. In CNT–NZF–CI layers these features show a minor but helpful magnetic contribution, while the main attenuation is dielectric.

Taken together, these diagnostics complement the preceding analyses. Once entrance matching is achieved ($|Z_{\text{in}}/Z_0| \approx 1$, Eq. (7)), the combined dielectric and magnetic pathways increase the attenuation constant α (Eq. (8)) and produce the observed minimum reflection loss and bandwidth.

Reflection loss (RL) is commonly used to characterize the microwave absorption properties of the samples. The RL values are expressed as a function of the normalized input impedance of a metal-backed absorber, as follows:

$$RL\ (dB) = 20\ log_{10}\left[\frac{(Z_{in}-1)}{(Z_{in}+1)}\right] \tag{5}$$

where Z_{in} is the normalized input impedance at the absorber surface and is given by:

$$Z_{in} = \left|\frac{Z_i}{Z_o}\right| = \sqrt{\frac{\mu_r}{\varepsilon_r}}\tan h\left(\frac{j2\pi\sqrt{\mu_r\varepsilon_r}}{c}\ fd\right) \tag{6}$$

Here, Z_i is the input impedance, Z_o is the free space impedance, d is the thickness of absorber, μ_r and ε_r have been described before, f is frequency, *and* c is the light velocity. The efficiency of a material in absorbing microwaves depends on two key factors. Effective impedance matching is a key requirement for optimal microwave absorption. The balance between permeability and permittivity is crucial in achieving impedance matching. A high degree of impedance matching, where $Z_{in} = Z_o$ indicates the material's ability to allow microwaves to penetrate and be efficiently converted into thermal energy or dissipated through interference. For optimal absorption, the input impedance of the absorbers (Z_{in}) and free space impedance (Z_o) must satisfy the following equation, ensuring the effective penetration of electromagnetic waves into the absorber:

$$Z_{in} = \left|\frac{Z_i}{Z_o}\right| \propto 1 \tag{7}$$

Second factor that contributes to efficient microwave absorber is strong attenuation capabilities, which are linked to various factors like complex permittivity, complex permeability, specific conductance, thickness, and absorber structure. These attributes ensure that electromagnetic waves can efficiently penetrate the material, minimizing reflection at interfaces. Reflections decrease when the absorber's characteristic impedance closely matched with that of free space. The attenuation constant α, which measures attenuation, can be described in terms of the dielectric and magnetic losses in an absorber using the

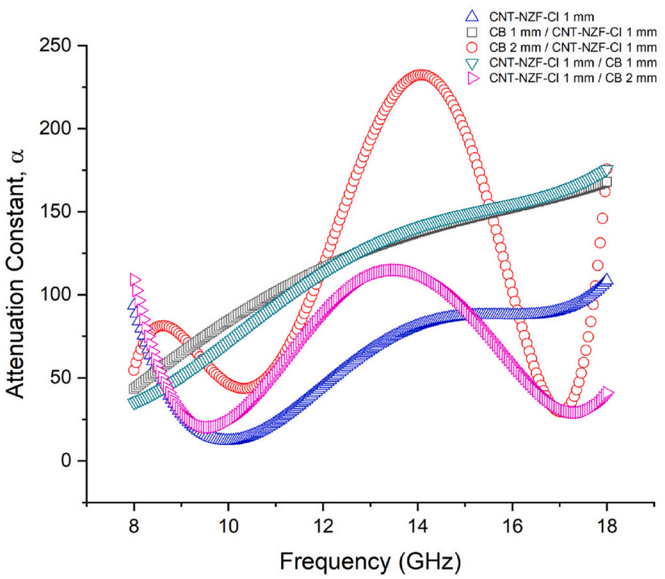

Fig. 11. Attenuation constant for single and double-layer nanocomposites structures.

following equation:

$$\alpha = \frac{\sqrt{2}\pi f}{c} \times \sqrt{(\mu''\varepsilon'' - \mu'\varepsilon') + \sqrt{(\mu''\varepsilon'' - \mu'\varepsilon')^2 + (\mu'\varepsilon'' - \mu''\varepsilon')^2}} \tag{8}$$

The reflection loss, normalized input impedance and attenuation constant for all samples are presented in Figs. 9, 10 and 11, respectively. Based on Fig. 9(a), single layer.

CNT-NZF-CI 1 mm shows poor performance of microwave absorber as compared to other samples and the microwave absorption does not even reach 90 % of absorption within the frequency range. The reason of such result is due to impedance mismatch, thus the electromagnetic wave that could not effectively penetrate the sample as the normalized input impedance, Z_{in} displayed a large value with maximum value of 37 (refer Figs. 10 and 11). Notably, Fig. 9(b) shows the 3D reflection loss plot for the CNT-NZF-CI 1 mm/CB 1 mm composite, which exhibited the best performance. The optimum matching thickness was determined using Equation (1), revealing a matching thickness of 2.1 mm at the frequency where the reflection loss is minimized.

Double-layer absorbers can be regarded as graded-impedance matching structures: an electromagnetic wave striking any interface reflects in proportion to the impedance mismatch between the incident and transmitting media. By making the impedance transition gradual across the coating, front-surface reflection is reduced. Practically, this means the air-facing layer should be relatively low-loss (moderate ε', controlled conductivity) to secure entrance matching $Z_{\text{in}}/\,Z_0| \approx 1$, while the subsequent layer should be lossier to provide strong internal attenuation. In our design, CNT-NZF-CI serves as the matching (front) layer and CB as the absorbing (back) layer, establishing a gentle impedance gradient from air to metal. A thin CNT network provides a continuous but tunable conduction pathway at low loading, yielding moderate ε' with controlled ε''. At the entrance, this reduces impedance mismatch, so

$Z_{\text{in}}/Z_0| \approx 1$ over a wider span and the wave can enter the coating. Once inside, the CNT network together with the CNT/CB interlayer boundary and magnetic centers (CI/NZF) in contact with the carbon network sustains additional loss channels. CB comprises nanocarbon aggregates with high defect and abundant interfaces (CB/epoxy and any residual magnetic species), which favour interfacial and dipolar polarization. Closely spaced CB particles act as micro-capacitive contacts, enabling charge accumulation and a large ε'' without excessively inflating ε'. CB agglomerates also promote multiple internal reflections in the interior. Positioning CB toward the backing therefore maximizes dissipation (higher α) after the wave has entered, while avoiding excess surface conductivity at the air interface.

This arrangement explains the sequence dependence of RL at 2 mm total thickness: with CNT-NZF-CI/CB, the entrance is well matched ($Z_{\text{in}}/Z_0| \approx 1$) and the field maximum resides in the lossier CB, yielding a deeper minimum (≈ -13 dB), whereas with CB/CNT-NZF-CI the entrance admittance is inflated ($Z_{\text{in}}/Z_0| \approx \approx 9$), reflection increases, and the minimum is shallower (≈ -10 dB). Significant variations in absorption were observed, with the CNT-NZF-CI serving as the matching layer achieving an absorption rate exceeding 99.99 % and conversely, when the position of the layers was switched and carbon black was used as the matching layer, the absorption exceeded 99.9 % but did not reach 99.99 %. The maximum absorption (minimum reflection loss) for both samples occurred at about the same range of frequency at around 11.0 and 11.14 GHz for CB 1 mm/CNT-NZF-CI 1 mm and CNT-NZF-CI 1 mm/CB 1 mm samples, respectively. Sample CNT-NZF-CI 1 mm/CB 1 mm offered a significant microwave absorption performance of −47.92 dB at 11.14 GHz while sample CB 1 mm/CNT-NZF-CI 1 mm demonstrated a significant microwave absorption of −37.01 dB at 11 GHz.

Another significant peak of absorption with more than 90 % was also observed at the frequency of 9.73 GHz for CB 1 mm/CNT-NZF-CI 1 mm sample. At this point of frequency, the sample exhibits good impedance matching (Z_{in} ~1 which represented by red-dashed line) and higher attenuation constant (refer Figs. 10 and 11). It was observed that absorption bandwidth at −10 dB (90 % absorption energy) was broadened for CNT-NZF-CI 1 mm/CB 1 mm sample as compared to that of similar sample but with the switched position of matching and absorbing layer. CNT-NZF-CI 1 mm/CB 1 mm and CB 1 mm/CNT-NZF-CI 1 mm samples demonstrated a significant absorption with an absorption bandwidth at −10 dB (90 % absorption) of 2.58 GHz and 2.29 GHz respectively. These results satisfied the conditions of efficient microwave absorber where the results are in agreement with the influence of impedance matching and attenuation factors as shown in Figs. 10 and 11 respectively. Based on Fig. 10, the normalized impedance, Z_{in} of both samples is close to 1, showing a good impedance matching. Moreover, the attenuation constant, α for both samples displayed significant values with slightest variation between both samples. The attenuation increased with increased frequency where CNT-NZF-CI 1 mm/CB 1 mm sample displayed a maximum attenuation of 176 CB 1 mm/CNT-NZF-CI 1 mm sample displayed attenuation of 167. Even though the attenuation constant for both samples were not the highest, as compared to other samples especially CB 1 mm/CNT-NZF-CI 1 mm sample, but the samples have good impedance matching which the samples must satisfy this condition first in order for the electromagnetic wave to penetrate the samples before getting attenuated. Based on literature [43], dielectric polarization will be increased with the amount of carbon black content as well as by higher surface area, which thus attenuating electromagnetic wave through reflection and multi-scattering. Furthermore, increasing the concentration of conductive particles per unit volume enhances the conductive network, which in turn facilitates wave attenuation through eddy currents. Interestingly, in this study, a thinner sample consisting of 1 mm carbon black exhibited superior microwave absorption properties, likely attributed to improved impedance matching afforded by the double-layer structure.

There is slightest and insignificant variation when the layer was switching from matching to absorbing layer and vice versa for samples with total thickness of 3 mm. It was found that as the carbon black layer increased to 2 mm, in which the total thickness of double-layer samples is 3 mm, the minimum reflection loss peak was not visible within the frequency range, regardless of the layer positions. This result is coherent with the equation shown in Equation (1), where the resonant frequency might shift to lower frequency correspond to the matching layer thickness, t_m. Based on Fig. 9(a), no effective absorption bands were observed in

CB 2 mm/CNT-NZF-CI 1 mm sample and CNT-NZF-CI 1 mm/CB 2 mm sample within the measured frequency range, suggested that the

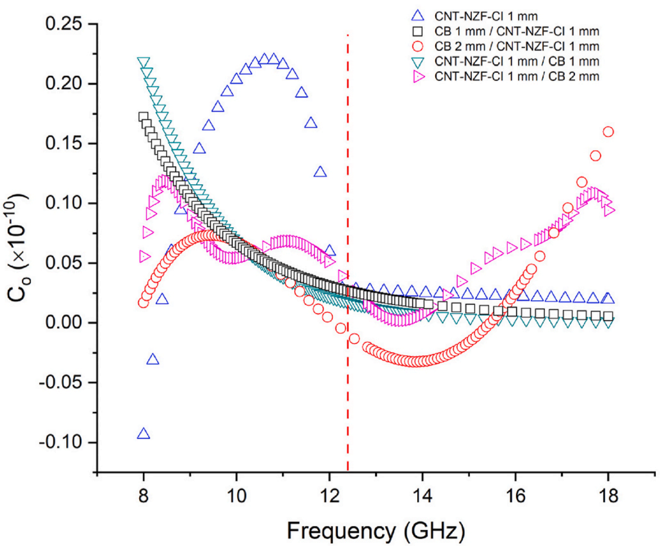

Fig. 12. Eddy current effect from 8 to 18 GHz.

minimum reflection loss might occurred at lower frequency due to the thickness of the absorber. This phenomenon can be attributed to quarter-wavelength attenuation, resulting from the phase inversion of the reflected microwaves at the upper and lower surfaces of the absorber [44]. Minimum reflection loss (highest absorption) was observed at frequency of 8 GHz for both samples in which the absorption hardly surpassed 90 % absorption. CNT-NZF-CI 1 mm/CB 2 mm sample displays minimum reflection loss of −13 dB while CB 2 mm/CNT-NZF-CI 1 mm sample displays −10 dB. At this particular frequency, the normalized input impedance, Z_{in} was nearly 1 when CNT-NZF-CI acted as matching layer, but reached 9 when carbon black is switching as matching layer, showing a poorer impedance mismatch. Further, the attenuation constant, α results in Fig. 11 reflects strong attenuation at 8 GHz for CNT-NZF-CI 1 mm/CB 2 mm sample as compared to CB 2 mm/CNT-NZF-CI 1 mm sample.

Eddy current loss, denoted as C_o, is primarily influenced by the thickness, d, and electrical conductivity, σ, of the nanocomposites. Thus, relationship can be expressed by the equation, $\mu'' (\mu')^{-2}f^{-1} = 2\pi\mu_0 d^2\sigma$, where μ_0 represents the permeability of free space [45]. It is important to note that the values of C_o should remain constant across varying frequencies, assuming that magnetic loss is solely attributable to the effects of eddy currents. Based on Fig. 12, the values of C_o for CNT-NZF-CI 1 mm/CB 2 mm sample and CB 2 mm/CNT-NZF-CI 1 mm sample are drastically fluctuated throughout the measured frequency while for CNT-NZF-CI 1 mm, the C_o values fluctuate in 8–12.4 GHz. This indicates that the eddy current effect is minimal and does not significantly contribute to magnetic loss within this frequency range. For both the CNT-NZF-CI 1 mm/CB 1 mm sample and CB 1 mm/CNT-NZF-CI 1 mm sample configurations, C_o values decreased with increasing frequency. Beyond approximately 12.4 GHz, the samples exhibited a more stable, plateau-like behavior, suggesting the onset of eddy current effects. According to this observation, we can infer that the resonance in all samples was predominantly driven by natural FMR across the studied frequency range. Furthermore, starting from 12.4 GHz (as marked by the red line in Fig. 12), eddy current loss became more pronounced in the CNT-NZF-CI 1 mm, CNT-NZF-CI 1 mm/CB 1 mm, and CB 1 mm/CNT-NZF-CI 1 mm samples, with C_o values stabilizing beyond 12 GHz.

Following the mechanism analysis above, we benchmark the present samples against representative ferrite nanoparticle and double-layer absorbers. Table 2 reports the material contents, total thickness, $RL_{\min}$, peak frequency, and −10 dB effective absorption bandwidth (EAB) for our samples and for relevant ferrites and hybrid systems cited here. The present 2 mm double-layer sample based on a CNT–NZF–CI matching layer and a carbon-black absorbing layer delivers a −10 dB bandwidth of 2.58 GHz with a very deep point absorption of more than 99.99 % (∼−40 dB) near 11.14 GHz. These values place our design in a favorable thickness–bandwidth trade-space relative to $CoFe_2O_4$/carbon hybrids at ∼2.5–3.0 mm and ferrite-coated CNT polymer composites at 3.0 mm, while avoiding the larger through-thickness required by full-band architected honeycombs. The comparison clarifies that our impedance-graded, material-only double-layer achieves competitive performance at lower total thickness by combining entrance matching through the CNT–NZF–CI front layer with interior attenuation in the carbon-black back layer.

Table 2
Literature benchmarks on ferrite nanoparticle/layered absorbers.

System	Architecture	Total thickness (mm)	Frequency, *f* at $RL_{\min}$ (GHz)	$RL_{\min}$ (dB)	EAB (GHz; band)	Notes	Source
This work	CNT–NZF–CI (front, matching)/CB (back, absorbing)	2.0 (1 + 1)	11.14	≈ −40 (≈99.99 %)	2.58 (−10 dB; X–Ku)	Thin double-layerr; graded impedance + magnetic-dielectric coupling	This study
This work	CNT–NZF–CI single layer	1.0	–	–	–	Control; X–K_u characterization	This study
Co-doped Ni–Zn ferrite on graphene (CNZF/GN)	Ferrite–graphene hybrid	3.1/4.6	9.6/5.2	−53.5/ −58.3	up to ∼14.8 (broad)	Dual regions; quarter-wave trend at moderate thickness	[31]
$CoFe_2O_4$/mesoporous carbon	Hybrid nanocomposite	2.5	11.4	−51	4.2 (K/Ka region)	Impedance matching + interfacial relaxation	[46]
$CoFe_2O_4$/N-doped rGO	$CoFe_2O_4$–N-rGO hybrid	2.5	11.4	−53.6	Broad (X–Ku; thickness-dependent)	Defect-rich carbon scaffolds distribute relaxations	[47]
$Ni_{1-x}Zn_xFe_2O_4$ (x = 0.2)	Ferrite pellets (single layer)	3.0	∼13.8	−31.17	–	Ku-band baseline; matching at RL minima	[48]
Ferrite-coated MWCNT/PVDF	MWCNT@ferrite in PVDF/ epoxy	3.0	8.5/9.6	to −35	3.9 (X-band)	Conductive network + soft-magnetic inclusions	[49]
rGO/non-woven honeycomb (single layer)	RGO fabric in honeycomb	5.0	–	−37	12.1 (5.9–18)	Structural multiple scattering; graded paths	[42]
rGO/non-woven honeycomb (bilayer)	Two-layer honeycomb	10.0	2–18	≤ −10 across band	Full 2–18 GHz	Structural impedance control; full-band coverage	[42]
CNT/CB/PU sandwich honeycomb	CBCNTs sandwich honeycomb	–	–	–	15.5 (≤−10 dB)	Wide EAB with mechanical robustness	[50]

4. Conclusion

In this work, CNTs have been synthesized through the chemical vapor deposition technique utilizing NZF and carbonyl iron as catalysts to create synergistic effects between dielectric and magnetic losses in the absorber. Composite absorbers with single- and double-layer configurations were fabricated by alternating the positions of the matching and absorbing layers. The CNT-NZF-CI 1 mm/CB 1 mm configuration achieved an absorption bandwidth of 2.58 GHz at −10 dB, with absorption exceeding 99.99 % at 11.4 GHz. The synergistic interactions between the dielectric and magnetic materials facilitated effective impedance matching and attenuation of EM waves, primarily through dielectric and magnetic losses, resulting in optimum absorption properties. The enhanced performance arises from synergistic dielectric–magnetic interactions, effective impedance matching, and strong attenuation mechanisms such as interfacial polarization, conductive loss, and multiple scattering within the CNT network. These findings demonstrate that combining CNT with carbon black in a dual-layer structure is an efficient for achieving lightweight, thin, and broadband microwave absorbers.

CRediT authorship contribution statement

Idza Riati Ibrahim: Writing – original draft, Validation, Investigation, Formal analysis, Data curation, Conceptualization. **Rodziah Nazlan:** Writing – review & editing, Validation, Investigation. **Siti Nor Ain Rusly:** Writing – review & editing, Investigation. **Fadzidah Mohd Idris:** Methodology, Investigation. **Khamirul Amin Matori:** Project administration, Funding acquisition, Conceptualization. **Ismayadi Ismail:** Methodology, Funding acquisition, Conceptualization. **Ghazaleh Bahmanrokh:** Writing – review & editing. **Muhammad Misbah Muhamad Zulkimi:** Methodology, Investigation. **Nor Hapishah Abdullah:** Investigation. **Muhammad Syazwan Mustaffa:** Investigation. **Arlina Ali:** Writing – review & editing, Validation.

Declaration of competing interest

The authors declare that they have no known competing financial interests or personal relationships that could have appeared to influence the work reported in this paper.

Acknowledgements

The authors acknowledge Universiti Malaysia Sarawak for supporting this project. This research has also received additional funding from the Ministry of Higher Education of Malaysia through the Long-Term Research Grant Scheme (LRGS/B-U/2013/UPNM/Defence & Security-P2) and from Universiti Malaysia Pahang Al-Sultan Abdullah through the Fundamental Internal Research Grant (RDU250319).

Data availability

Data will be made available upon request.

References

[1] J. Huo, L. Wang, H. Yu, Polymeric nanocomposites for electromagnetic wave absorption, J. Mater. Sci. 44 (2009) 3917–3927, https://doi.org/10.1007/s10853-009-3561-1.

[2] L.L. Adebayo, H. Soleimani, N. Yahya, Z. Abbas, F.A. Wahaab, R.T. Ayinla, H. Ali, Recent advances in the development OF Fe3O4-BASED microwave absorbing materials, Ceram. Int. 46 (2020) 1249–1268, https://doi.org/10.1016/j.ceramint.2019.09.209.

[3] Z. Zhao, Y. Qing, L. Kong, H. Xu, X. Fan, J. Yun, L. Zhang, H. Wu, Advancements in microwave absorption motivated by interdisciplinary research, Adv. Mater. 36 (2024), https://doi.org/10.1002/adma.202304182.

[4] M. Green, X. Chen, Recent progress of nanomaterials for microwave absorption, J. Materiomics 5 (2019) 503–541, https://doi.org/10.1016/j.jmat.2019.07.003.

[5] A.H. Najafabadi, A. Ghasemi, R. Mozaffarinia, Development of novel magnetic-dielectric ceramics for enhancement of reflection loss in X band, Ceram. Int. 42 (2016) 13625–13634, https://doi.org/10.1016/j.ceramint.2016.05.157.

[6] F. Mohd Idris, M. Hashim, Z. Abbas, I. Ismail, R. Nazlan, I.R. Ibrahim, Recent developments of smart electromagnetic absorbers based polymer-composites at gigahertz frequencies, J. Magn. Magn Mater. 405 (2016) 197–208, https://doi.org/10.1016/j.jmmm.2015.12.070.

[7] M. Kallumottakkal, M.I. Hussein, M.Z. Iqbal, Recent progress of 2D nanomaterials for application on microwave absorption: a comprehensive study, Front. Mater. 8 (2021) 1–19, https://doi.org/10.3389/fmats.2021.633079.

[8] I.R. Ibrahim, K.A. Matori, I. Ismail, Z. Awang, S. Nor, A. Rusly, R. Nazlan, F. M. Idris, M. Misbah, M. Zulkimi, N.H. Abdullah, M.S. Mustaffa, F.N. Shafiee, M. Ertugrul, A study on microwave absorption properties of carbon Black and by Ni0.6Zn0.4Fe2O4 nanocomposites tuning the matching-absorbing layer structures, Sci. Rep. 10 (2020) 1–14, https://doi.org/10.1038/s41598-020-60107-1.

[9] P. Ranjan, A. Choubey, S.K. Mahto, A novel approach for optimal design of multilayer wideband microwave absorber using wind driven optimization technique, AEU - International Journal of Electronics and Communications 83 (2018) 81–87, https://doi.org/10.1016/j.aeue.2017.08.039.

[10] Z. Du, X. Chen, Y. Zhang, X. Que, P. Liu, X. Zhang, H.L. Ma, M. Zhai, One-pot hydrothermal preparation of Fe3O4 decorated graphene for microwave absorption, Materials 13 (2020) 1–12, https://doi.org/10.3390/ma13143065.

[11] Z. Hou, J. Xiang, X. Zhang, L. Gong, J. Mi, X. Shen, K. Zhang, Microwave absorption properties of single- and double-layer absorbers based on electrospun nickel–zinc spinel ferrite and carbon nanofibers, J. Mater. Sci. Mater. Electron. 29 (2018) 12258–12268, https://doi.org/10.1007/s10854-018-9338-z.

[12] A. Houbi, Z.A. Aldashevich, Y. Atassi, Z. Bagasharova Telmanovna, M. Saule, K. Kubanych, Microwave absorbing properties of ferrites and their composites: a review, J. Magn. Magn Mater. 529 (2021) 167839, https://doi.org/10.1016/j.jmmm.2021.167839.

[13] W. Ma, R. Yang, Z. Yang, C. Duan, T. Wang, Synthesis of reduced graphene oxide/zinc ferrite/nickel nanohybrids: as a lightweight and high-performance microwave absorber in the low frequency, J. Mater. Sci. Mater. Electron. 30 (2019) 18496–18505, https://doi.org/10.1007/s10854-019-02203-1.

[14] R. Shu, J. Zhang, C. Guo, Y. Wu, Z. Wan, J. Shi, Y. Liu, M. Zheng, Facile synthesis of nitrogen-doped reduced graphene oxide/nickel-zinc ferrite composites as high-performance microwave absorbers in the X-band, Chem. Eng. J. 384 (2020) 123266, https://doi.org/10.1016/j.cej.2019.123266.

[15] A.K.M.A. Hossain, S.T. Mahmud, M. Seki, T. Kawai, H. Tabata, Structural, electrical transport, and magnetic properties of Ni1-xZnxFe2O4, J. Magn. Magn Mater. 312 (2007) 210–219, https://doi.org/10.1016/j.jmmm.2006.09.030.

[16] S.N.A. Rusly, I. Ismail, K.A. Matori, Z. Abbas, A.H. Shaari, Z. Awang, I.R. Ibrahim, F.M. Idris, M.H. Mohd Zaid, M.K.A. Mahmood, I.H. Hasan, Influence of different BFO filler content on microwave absorption performances in BiFeO3/epoxy resin composites, Ceram. Int. 46 (2020) 737–746, https://doi.org/10.1016/J.CERAMINT.2019.09.027.

[17] P. Yin, L. Zhang, X. Feng, J. Wang, J. Dai, Y. Tang, Recent progress in ferrite microwave absorbing composites, Integrated Ferroelectrics Int. J. 211 (2020) 82–101, https://doi.org/10.1080/10584587.2020.1803677.

[18] A. Verma, R.G. Mendiratta, T.C. Goel, D.C. Dube, Microwave studies on Strontium ferrite based absorbers, J. Electroceram. 8 (2002) 203–208.

[19] Y. Meng, Q. Qian, Y. Liu, L.B. Kong, Ni1−xZnxFe2O4/coal-based carbon composites with tunable electromagnetic wave absorption properties prepared with microwave irradiation and hydrothermal reaction, Colloids Surf. A Physicochem. Eng. Asp. 683 (2024) 133019, https://doi.org/10.1016/j.colsurfa.2023.133019.

[20] M.S. Mustaffa, R.S. Azis, N.H. Abdullah, I. Ismail, I.R. Ibrahim, An investigation of microstructural, magnetic and microwave absorption properties of multi-walled carbon nanotubes/Ni0.5Zn0.5Fe2O4, Sci. Rep. 9 (2019) 15523, https://doi.org/10.1038/s41598-019-52233-2.

[21] N. Rosdi, R.S. Azis, I. Ismail, N. Mokhtar, M.M. Muhammad Zulkimi, M.S. Mustaffa, Structural, microstructural, magnetic and electromagnetic absorption properties of spiraled multiwalled carbon nanotubes/barium hexaferrite (MWCNTs/BaFe12O19) hybrid, Sci. Rep. 11 (2021) 15982, https://doi.org/10.1038/s41598-021-95332-9.

[22] L. Guo, Y. He, D. Chen, B. Du, W. Cao, Y. Lv, Z. Ding, Hydrothermal synthesis and microwave absorption properties of nickel ferrite/multiwalled carbon nanotubes composites, Coatings 11 (2021) 534, https://doi.org/10.3390/coatings11050534.

[23] C. Hu, H. Liu, Y. Zhang, M. Zhang, J. Yu, X. Liu, X. Zhang, Tuning microwave absorption properties of multi-walled carbon nanotubes by surface functional groups, J. Mater. Sci. 54 (2019) 2417–2426, https://doi.org/10.1007/s10853-018-2895-y.

[24] S.K. Singh, M.J. Akhtar, K.K. Kar, Hierarchical carbon nanotube-coated carbon fiber: Ultra lightweight, thin, and highly efficient microwave absorber, ACS Appl. Mater. Interfaces 10 (2018) 24816–24828, https://doi.org/10.1021/acsami.8b06673.

[25] X. Chen, H. Liu, D. Hu, H. Liu, W. Ma, Recent advances in carbon nanotubes-based microwave absorbing composites, Ceram. Int. 47 (2021) 23749–23761, https://doi.org/10.1016/j.ceramint.2021.05.219.

[26] B. Jiang, C. Qi, H. Yang, X. Wu, W. Yang, C. Zhang, S. Li, L. Wang, Y. Li, Recent advances of carbon-based electromagnetic wave absorption materials facing the actual situations, Carbon N Y 208 (2023) 390–409, https://doi.org/10.1016/j.carbon.2023.04.002.

[27] A. Saib, L. Bednarz, R. Daussin, C. Bailly, X. Lou, J.-M. Thomassin, C. Pagnoulle, C. Detrembleur, R. Jérôme, I. Huynen, Carbon nanotube composites for broadband

microwave absorbing materials, IEEE Trans Microw Theory Tech 54 (2006) 2745–2754, https://doi.org/10.1109/Tntt.2006.0874889.

[28] S. Kumar, R. Walia, A. Kumar, V. Verma, Hybrid structure of MWCNT/Ferrite and GO incorporated composites for microwave shielding properties and their practical applications, RSC Adv. 11 (2021) 9775–9787, https://doi.org/10.1039/D1RA01129D.

[29] A. Ling, G. Tan, Q. Man, Y. Lou, S. Chen, X. Gu, R.-W. Li, J. Pan, X. Liu, Broadband microwave absorbing materials based on MWCNTs' electromagnetic wave filtering effect, Compos. B Eng. 171 (2019) 214–221, https://doi.org/10.1016/j.compositesb.2019.04.034.

[30] M. Bibi, S.M. Abbas, N. Ahmad, B. Muhammad, Z. Iqbal, U.A. Rana, S.U.-D. Khan, Microwaves absorbing characteristics of metal ferrite/multiwall carbon nanotubes nanocomposites in X-band, Compos. B Eng. 114 (2017) 139–148, https://doi.org/10.1016/j.compositesb.2017.01.034.

[31] P. Liu, Z. Yao, J. Zhou, Z. Yang, L.B. Kong, Small magnetic Co-doped NiZn ferrite/graphene nanocomposites and their dual-region microwave absorption performance, J Mater Chem C Mater 4 (2016) 9738–9749, https://doi.org/10.1039/c6tc03518c.

[32] P. Liu, V. Ming, H. Ng, Z. Yao, J. Zhou, Y. Lei, Z. Yang, H. Lv, L.B. Kong, Facile synthesis and hierarchical assembly of flower-like NiO structures with enhanced dielectric and microwave absorption properties. http://pubs.acs.org, 2017.

[33] P. Liu, Z. Yao, V.M.H. Ng, J. Zhou, L.B. Kong, K. Yue, Facile synthesis of ultrasmall Fe3O4 nanoparticles on MXenes for high microwave absorption performance, Compos Part A Appl Sci Manuf 115 (2018) 371–382, https://doi.org/10.1016/j.compositesa.2018.10.014.

[34] I.R. Ibrahim, M. Hashim, R. Nazlan, I. Ismail, W.N. Wan Ab Rahman, N. H. Abdullah, F. Mohd Idris, M.S.E. Shafie, M.M. Muhamad Zulkimi, Grouping trends of magnetic permeability components in their parallel evolution with microstructure in $Ni_{0.3}Zn_{0.7}Fe_2O_4$, J. Magn. Magn Mater. 355 (2014), https://doi.org/10.1016/j.jmmm.2013.12.024.

[35] A. Jorio, E.H.M. Ferreira, M.V.O. Moutinho, F. Stavale, C.A. Achete, R.B. Capaz, Measuring disorder in graphene with the G and D bands, Phys. Status Solidi 247 (2010) 2980–2982, https://doi.org/10.1002/pssb.201000247.

[36] X. Liu, J. Choi, Z. Xu, C.P. Grey, S. Fleischmann, A.C. Forse, Raman spectroscopy measurements support disorder-driven capacitance in nanoporous carbons, J. Am. Chem. Soc. 146 (2024) 30748–30752, https://doi.org/10.1021/jacs.4c10214.

[37] S.-R. Cho, H.-G. Cho, Characterization of black carbon collected from candle light and automobile exhaust pipe, J. Kor. Chem. Soc. 57 (2013) 691–696, https://doi.org/10.5012/jkcs.2013.57.6.691.

[38] Y. Yan, J. Zhou, J. Tao, L. Duan, Y. Liu, Z. Cheng, Y. Wang, Z. Liu, Z. Ning, X. Wang, X. Tao, P. Liu, Z. Yao, Regulating growth kinetics of carbon nanotubes toward efficient microwave absorption, Small 21 (2025), https://doi.org/10.1002/smll.202410799.

[39] D. Li, Y. Feng, D.S. Pan, L.W. Jiang, Z.M. Dai, S.J. Li, Y. Wang, J. He, W. Liu, Z. D. Zhang, Negative imaginary parts of complex permeability and microwave absorption performance of core double-shelled FeCo/C/Fe2.5Cr0.5Se4nanocomposites, RSC Adv. 6 (2016) 73020–73027, https://doi.org/10.1039/c6ra12772j.

[40] I.R. Ibrahim, K.A. Matori, I. Ismail, Z. Awang, S. Nor, A. Rusly, R. Nazlan, F. M. Idris, M. Misbah, M. Zulkimi, N.H. Abdullah, M.S. Mustaffa, F.N. Shafiee, M. Ertugrul, A study on microwave absorption properties of carbon black and by Ni0.6Zn0.4Fe2O4 nanocomposites tuning the matching-absorbing layer structures, Sci. Rep. 10 (2020) 1–14, https://doi.org/10.1038/s41598-020-60107-1.

[41] Z. Zhang, Z. Lu, N. Liu, X. Gao, L. Li, R. Hu, Enhanced low-frequency electromagnetic wave absorption and corrosion resistance of flaky carbonyl iron particles via atomic layer deposition of Al2O3 nanocoatings, Ceram. Int. 51 (2025) 41191–41204, https://doi.org/10.1016/j.ceramint.2025.06.342.

[42] H. Li, S. Bi, J. Cai, X. Chu, G. Hou, J. Zhang, T. Wu, Reduced graphene oxide/nonwoven fabric filled honeycomb composite structure for broadband microwave absorption, Carbon N Y 223 (2024) 119005, https://doi.org/10.1016/j.carbon.2024.119005.

[43] P. Mehdizadeh, H. Jahangiri, Effect of carbon black content on the microwave absorbing properties of CB/epoxy composites, Journal of Nanostuctures 6 (2016) 140–148, https://doi.org/10.7508/jns.2016.02.006.

[44] J. Luo, L. Yue, H. Ji, K. Zhang, N. Yu, Investigation on the optimization, design and microwave absorption properties of BaTb0.2Eu0.2Fe11.6O19/PANI decorated on reduced graphene oxide nanocomposites, J. Mater. Sci. 54 (2019) 6332–6346, https://doi.org/10.1007/s10853-018-03305-7.

[45] X. Zhou, D. Chuai, D. Zhu, Electrospun synthesis of reduced graphene oxide (RGO)/NiZn ferrite nanocomposites for excellent microwave absorption properties, J Supercond Nov Magn 32 (2019) 2687–2697, https://doi.org/10.1007/s10948-019-5039-y.

[46] D. Chaudhary, P. Pantola, S. Kumar, P. Agarwal, B.K. Kuanr, Synthesis of a lightweight and dual-band (K and Ka-band) microwave absorber based on cobalt ferrite/mesoporous carbon nanocomposite for stealth technology, Ceram. Int. 51 (2025) 1115–1123, https://doi.org/10.1016/j.ceramint.2024.11.093.

[47] P. Anil, A. Joseph, B. Arun, K.C.J. Raju, V.V.R.K. Kumar, Enhanced X-band microwave absorption properties of cobalt ferrite/nitrogen-doped rGO nanocomposites, Mater. Sci. Eng., B 323 (2025), https://doi.org/10.1016/j.mseb.2025.118859.

[48] N. Aggarwal, S.B. Narang, Magnetic characterization of nickel-zinc spinel ferrites along with their microwave characterization in Ku band, J. Magn. Magn Mater. 513 (2020) 167052, https://doi.org/10.1016/j.jmmm.2020.167052.

[49] S.H. Siddiki, S. Das, K. Verma, L. Dashairya, S. Das, V.K. Thakur, G.C. Nayak, Substituted nickel ferrite coated MWCNT/PVDF based epoxy nanocomposite for microwave absorption, Ceram. Int. 48 (2022) 30260–30271, https://doi.org/10.1016/j.ceramint.2022.06.299.

[50] S. Bi, Y.Z. Song, G.L. Hou, H. Li, Z.H. Liu, Z.L. Hou, J. Zhang, Sandwich nanoarchitectonics of heterogenous CB/CNTs honeycomb composite for impedance matching design and microwave absorption, J. Alloys Compd. 943 (2023) 169154, https://doi.org/10.1016/j.jallcom.2023.169154.